Lyve-1 expressing perivascular macrophages orchestrate pericyte expansion to sustain angiogenesis in cancer

James W. Opzoomer[1], Joanne E. Anstee[1], Isaac Dean[2], Emily J. Hill[1], Ihssane Bouybayoune[1], Jonathan Caron[1], Tamara Muliaditan[1], Peter Gordon[1], Rosamond Nuamah[3], Sarah E. Pinder[1], Tony Ng[1], Francesco Dazzi[1], Shahram Kordasti[4], David R. Withers[2], Toby Lawrence[5,6,7] and James N. Arnold[1]

[1]School of Cancer and Pharmaceutical Sciences, King's College London, Faculty of Life Sciences and Medicine, Guy's Hospital, London, SE1 1UL, United Kingdom.

[2]Institute of Immunology and Immunotherapy, College of Medical and Dental Sciences, University of Birmingham, B15 2TT, United Kingdom.

[3]NIHR BRC Genomics Facility, Guy's and St Thomas' NHS Foundation Trust, King's College London, Guy's Hospital, SE1 9RT, United Kingdom.

[4]Department of Haematological Medicine, King's College London, School of Cancer and Pharmaceutical Sciences, Faculty of Life Sciences and Medicine, Denmark Hill, London, SE5 9NU, United Kingdom.

[5]Centre for Inflammation Biology and Cancer Immunology, School of Immunology & Microbial Sciences, King's College London, Faculty of Life Sciences and Medicine, Guy's Hospital, London, SE1 1UL, United Kingdom.

[6]Aix Marseille University, CNRS, INSERM, CIML, Marseille, France.

[7]Henan Key Laboratory of Immunology and Targeted Therapy, School of Laboratory Medicine, Xinxiang Medical University, Xinxiang, China.

Keywords

Macrophage, fibroblast, pericyte, stroma, tumor, angiogenesis

Abstract

Tumor associated macrophages (TAMs) are a highly plastic stromal cell type which are exquisitely polarized by the tumor microenvironment to support cancer progression [1, 2]. Single-cell RNA-sequencing (scRNA-seq) of TAMs from a spontaneous murine model of mammary adenocarcinoma (*MMTV-PyMT*) identified three distinct polarization trajectories for these cells within the tumor microenvironment. We reveal sub-divisions within the pro-tumoral TAM population with one subset expressing Lyve-1 and residing in a spatial niche proximal to blood vasculature within the tumor. We demonstrate that selective depletion of the Lyve-1^{+} TAM population significantly slows tumor growth because of a non-redundant role of these cells in orchestrating the platelet derived growth factor-CC (PDGF-CC)-dependent expansion of tumor-resident pericytes which underpins vasculature growth and development. This study uncovers that local pericyte expansion in cancer is not an autonomous event but tightly regulated by the perivascular Lyve-1^{+} TAM population, which ultimately govern the success of angiogenesis in cancer.

Results

TAMs form a major part of the stromal cell infiltrate in solid tumors [3]. Phenotypic and functional diversity in the TAM population has been widely characterized and their plastic nature is exploited by the tumor to facilitate disease progression through promoting angiogenesis [4, 5], immune suppression [6, 7], chemotherapeutic resistance [8, 9, 10] and tumor cell migration and metastasis [1, 11, 12, 13, 14, 15]. Although macrophage polarization has a spectrum of possible phenotypes that can be adopted [16, 17], it is apparent that functionally important subsets preferentially accumulate, that are guided by spatial and environmental cues, to conduct specialized tasks vital to tumor progression [1, 6 17, 18, 19, 20]. To resolve the heterogeneity of the TAM population, CD45^{+}Ly6G^{-}CD11b^{+}F4/80^{hi} TAMs were cell sorted by flow cytometry from enzyme-dispersed tumors from *MMTV-PyMT* mice [21] (Supplementary Fig. 1a). The TAMs were then subjected to the droplet-based 10X Genomics Platform for scRNA-seq (Fig. 1a). A total of 9,039 TAMs were sequenced across three individual tumors. Unsupervised graph-based clustering of the transcriptomes, visualized using *UMAP* [22], revealed eight distinct transcriptomic TAM clusters (Fig. 1b-d and Supplementary Fig. 1b,c). The presence of these transcriptomic clusters, despite the tumors being spontaneous, were conserved across the three tumors analyzed (Fig. 1e). Gene Ontology (GO) analysis of the transcriptional programs within these clusters revealed diversity in both the number and type of biological pathways that were active, with one cluster (TAM08) representing a highly proliferative TAM state (Fig. 1f and Supplementary Fig. 1d), suggesting that at least some TAM populations are potentially capable of self-renewal. Interestingly, the TAM clusters that

appeared to be the least polarized (TAM01 and 02), with few enriched GO terms, represented almost a quarter of TAMs within the tumor (23.3% ± 3.4 of all TAMs analyzed), suggesting that a significant proportion of TAMs remain relatively unspecialized in their role (Fig. 1e,f and Supplementary Fig. 1e). Trajectory analysis using *Slingshot* [23] and diffusion maps was able to align the 8 identified clusters into a three trajectory polarization model with TAM04, 06 and 07 clusters representing predicted polarization extremes (Fig. 1g,h and Supplementary Fig. 2). Analysis of the three developmental pathways for their enrichment of M1/M2 [24] programs using the marker gene list of Orecchioni *et al* [25] highlighted TAM04 to be skewed towards an inflammatory (M1-like) transcriptome (Fig. 2a,b) which were more enriched for expression of inflammatory genes representative of a cellular response to type-1 interferons such as *Irf7* and *Isg15.* TAM06 and TAM07 possessed a more pro-tumoral (M2-like) transcriptome (Fig. 2a,b). TAM06 was more enriched for anti-inflammatory genes such as *Il10,* whereas both TAM06 and TAM07 were enriched in *Ccl2*, *Mmp19* and *Hb-egf*. TAM06 and TAM07, the two pro-tumoral TAM programs, both also commonly expressed *Mrc1* (the gene for MRC1/CD206) [26], but were functionally distinct in many of their enriched GO biological pathways, with a preferential skewing of TAM06 towards angiogenic processes and TAM07 towards immune regulation, highlighting a specialized sub-division of roles within the tumor (Fig. 2c,d). Using flow cytometry analysis of gated CD206$^+$F4/80^{hi} TAMs stained for markers identified within the scRNA-seq analysis, confirmed that similar TAM sub-populations could be distinguished using the predicted protein markers in *MMTV-PyMT* tumors. The CD206 expressing pro-tumoral TAMs could be differentiated based on their expression level of CD206, MHCII, and the lymphatic vessel endothelial hyaluronic acid receptor 1 (Lyve-1) (Fig. 2e,f), into CD206^{lo}MHCII^{lo}Lyve-1$^-$ (TAM05) and the predicted polarization extremes of CD206^{hi}MHCII^{lo}Lyve-1$^+$ (TAM06) and CD206^{int}MHCII^{hi}Lyve-1$^-$ (TAM07) population. Lyve-1 has traditionally been considered a marker of lymphatic endothelium [27], but has also been utilized as a marker on tissue-resident macrophages [28, 29, 30, 31, 32] and TAMs [33]. The Lyve-1$^+$ subset (TAM06) accounted for 10.7±3.5% of TAMs and 1.4±0.4% of live cells within the tumor (Fig. 2g).

To validate that the populations identified in the scRNA-seq and flow cytometry data were equivalent, the FACs-gated populations were subjected to bulk population RNA-seq alongside CD206$^-$MHC^{lo}F4/80^{hi} TAMs as a comparator group. Principal component (PC) analysis confirmed these populations to be transcriptionally distinct (Fig. 2h,i). Comparing the bulk population RNA-seq to that of the scRNA-seq populations validated close concordance between the identified populations across a range of predicted marker genes (Fig. 2j). CD206^{hi}MHCII^{lo}Lyve-1$^+$ (TAM06) also selectively expressed the transcription factor *Maf* (Supplementary Fig. 2d) and CD206^{int}MHCII^{hi}Lyve-1$^-$ (TAM07) the transcription factor

Retnla (Fig. 1d), which may indicate that these transcription factors play a role in polarization identity. A monocyte-derived macrophage with a similar MHCII^{lo}Lyve-1^{hi} surface phenotype has been demonstrated to reside proximal to vasculature in a variety of healthy tissues [32]. The GO pathway analysis also suggested that CD206^{hi}MHCII^{lo}Lyve-1^{+} TAMs were highly endocytic (Fig. 2c). Liposomes containing the fluorescent lipophilic dye 1'-dioctadecyl-3,3,3',3''tetramethylindocarbocyanine perchlorate (DiI) have previously been used to study perivascular TAM (PvTAM) development [13] and we predicted they could represent a tool to specifically label the CD206^{hi}MHCII^{lo}Lyve-1^{+} TAM subset. We developed a labelling protocol that could selectively mark PvTAMs, rather than a monocytic progenitor (Supplementary Fig. 3a). Confocal analysis of the tumors demonstrated that DiI-liposomes labelled a population of PvTAMs (Fig. 2k-m) and *ex vivo* characterization of the DiI-labelled cells in enzyme-dispersed tumors confirmed their phenotype to indeed be that of the CD206^{hi}MHCII^{lo}Lyve-1^{+} TAM (TAM06, Fig. 2n).

As the liposome labeling protocol preferentially labelled CD206^{hi}MHCII^{lo}Lyve-1^{+} TAMs (Fig. 2m,n and Supplementary Fig. 3a), we utilized clodronate-filled liposomes [34] under an equivalent administration protocol as a means to selectively deplete the population and investigate their possible role in tumor progression. Depletion of these cells in *MMTV-PyMT* tumors resulted in a significant slowing of tumor growth (Fig. 3b), highlighting a fundamental role for these cells in tumor progression. *Ex vivo* analysis of the tissues revealed that clodronate-filled liposomes efficiently depleted the splenic macrophages (Supplementary Fig. 3b), with little sign of toxicity in the animals (Supplementary Fig. 3c). However, even over the long-term administration of clodronate-filled liposomes, the selective nature of the depletion of CD206^{hi}MHCII^{lo}Lyve-1^{+} (TAM06) TAMs was maintained, sparing the CD206^{int}MHCII^{hi}Lyve-1^{-} (TAM07) subset of specialized pro-tumoral TAMs (Fig. 3c-e), CD206^{-} TAMs, (Fig. 3f) and CD11b^{+}Ly6C^{+} monocytes (Fig. 3g). Furthermore, using immunofluorescence imaging there was an observable selective spatial loss of PvTAMs within the clodronate-filled liposome treated mice (Fig. 3h), where clusters of TAMs surrounding blood vessels were no longer observable. To understand the mechanism through which CD206^{hi}MHCII^{lo}Lyve-1^{+} TAMs promote tumor progression (Fig. 3b), we first phenotyped the immune-infiltrate of the tumors, however there was no associated change in abundance of any immune cell population analyzed within the tumor microenvironment, other than a statistically significant increase in the abundance of the migratory CD11c^{+}CD103^{+}dendritic cells (DCs) (Fig. 3i), which contribute to cytotoxic T-lymphocyte recruitment in the tumor [35] and priming of the anti-tumor immune response [36]. However, there was no increase in CD8^{+} or CD4^{+} T-cell recruitment in the absence of CD206^{hi}MHCII^{lo}Lyve-1^{+} TAMs (Fig. 3i). Due to the Pv location of CD206^{hi}MHCII^{lo}Lyve-1^{+}

TAMs, it was possible that these cells may play a central role in promoting neo-angiogenesis to sustain tumor growth [37, 38]. Immunofluorescence analysis of sections from *MMTV-PyMT* tumors stained for CD31$^+$ endothelial cells and perivascular α-smooth muscle actin (αSMA) expressing stromal cells (Fig. 3j), revealed no significant change in the overall proportion of endothelial cells (Fig. 3k) and a small, but significant, increase in vessel density (Supplementary Fig. 3d) in the tumor. However, there was a striking loss of αSMA$^+$ stromal cells proximal to vasculature (Fig. 3j,l). Although there is evidence that mesenchymal populations can be phagocytic [39], neither CD45$^-$CD31$^+$ endothelial cells nor CD45$^-$CD90$^+$ mesenchymal stromal cells [40] had up-taken the liposomes (Supplementary Fig. 3e), excluding any direct killing effect of the clodronate on these populations. This however, highlighted a potential role of CD206^{hi}MHCII^{lo}Lyve-1$^+$ TAMs in maintenance of the αSMA$^+$ stromal population.

Staining tissue sections from *MMTV-PyMT* tumors for αSMA$^+$ cells and F4/80$^+$ TAMs placed these populations in the same perivascular 'niche' with a close spatial arrangement providing opportunity for interactions (Fig. 4a). This colocalization was also evident in human invasive breast carcinomas, where CD68$^+$ TAMs and αSMA$^+$ cells could be found in close proximity adjacent to CD31$^+$ endothelial cells lining blood vessels (Fig. 4b). Interestingly, this relationship was not observed in ductal carcinoma *in situ* (DCIS), suggesting that the spatial arrangement could be associated with progressive disease where there is ongoing neo-angiogenesis (Fig. 4b). To further investigate these perivascular αSMA$^+$ cells, we characterized the heterogeneity of a broad pool of tumor-associated mesenchymal stromal cells (collectively termed cancer associated fibroblasts; CAFs) that were CD45$^-$CD31$^-$CD90$^+$ using flow cytometry within enzyme-dispersed *MMTV-PyMT* tumors. The CD45$^-$CD90$^+$ CAF population accounted for 4.0±1.6% of total live cells within 350mm^3 tumors and their abundance increased as tumors progressed (Fig. 4c). We screened the CD45$^-$CD90$^+$ CAFs [40] for cell surface markers identified as being associated with CAFs [40, 41] including; Ly6a, CD34, PDGFRα, FAP and CD29 [42, 43]. Clustering of the multi-parametric flow cytometry data using *UMAP* [22] and FlowSOM [44] distinguished two distinct subsets (Fig. 4d) and these two populations could be separated based on their expression of CD34 (Fig. 4e). To identify the αSMA-expressing population and further characterize the functionality of these cells, we subjected CD34$^+$ and CD34$^-$ CAFs to bulk RNA-seq. This analysis demonstrated clear transcriptional differences in these CAF subsets (Supplementary Fig. 4a-c), with the CD34$^-$ CAFs, in addition to expressing αSMA (*Acta2*), also expressing *Des, Pdgfrb* and *Cspg4* (Fig. 4f) which are genes associated with pericytes, a population of specialized vessel associated mesenchymal cells [45]. To confirm the presence of Desmin (*Des*) and NG2 (*Cspg4*) at the protein level in these cells, immunofluorescence staining of tissues sections from *MMTV-*

PyMT mice confirmed that the Pv αSMA[+] CAFs were also Desmin[+] (Supplementary Fig. 4d), and *ex vivo* flow cytometry confirmed the presence of surface NG2 (Supplementary Fig. 4e). Alongside their proximity to vasculature, we elected to refer to these cells as 'pericytes'. Analyzing the abundance of pericytes over the different stages of tumor progression from the healthy mammary gland, hyperplasia and the growing tumor revealed a relative increase in the abundance of the population within the CAF population over tumor progression, suggesting a selection of this subset within the tumor microenvironment (Fig. 4g). Analyzing the identified CAF populations across different ectopic tumor models including B16, LL2 and orthotopic 4T1, demonstrated these cell populations to be present in all tumor models analyzed (Supplementary Fig. 4f,g). The progenitor of pericytes/CAF populations still remain debated in cancer, and may originate from different sources [46]. To elucidate the route through which these cells were accumulating in the tumor, we first explored local proliferation and pulsed mice bearing *MMTV-PyMT* tumors with 5-ethynyl-2'-deoxyuridine (Edu) to label actively proliferating cells. Although both CD34^{+} CAFs and pericyte populations displayed evidence of proliferation by comparison with healthy mammary gland, the pericytes were proliferating at a significantly faster rate (Fig. 4h). To exclude recruitment and address whether the proliferation of the pericytes was sufficient to account for their preferential expansion with tumor growth we utilized the *Kaede* mouse [47] crossed to the *MMTV-PyMT* model. Using this approach, we were able to photoconvert all tumor and stromal cells within a 100mm[3] tumor from *Kaede*-green to *Kaede*-red (Fig. 4i). Analyzing tumors 72h after photoconversion demonstrated that CD45^{+} stromal cells predominantly displayed Kaede-green, highlighting the continual recruitment of hematopoietic stromal cells to the tumor from the periphery[13, 48, 49, 50]. In contrast, both pericyte and CD34^{+} CAFs remained *Kaede* red, which indicated that the expansion of this population was solely from tumor-resident cells and not dependent on a peripheral source (Fig. 4i). The rapid proliferation of the pericytes relative to the CD34^{+} CAF also explains the dynamics within the CD90^{+} mesenchymal stromal compartment over tumor growth (Fig. 4g).

Immunofluorescence analysis for Ki67, a marker of proliferation [51], on αSMA^{+} cells confirmed a close spatial relationship between proliferating Ki67^{+}αSMA[+] pericytes and F4/80[+] PvTAMs (Fig. 4j). Pericytes have previously been shown to sense inflammation and attract and interact with macrophages [52, 53]. However, the biological implications of this interaction are largely unknown. To investigate whether CD206^{hi}MHCII^{lo}Lyve-1^{+} PvTAMs might be implicated in the expansion of pericytes to sustain the angiogenic requirements of the tumor, we analyzed the incorporation of Edu in the presence and absence of CD206^{hi}MHCII^{lo}Lyve-1^{+} PvTAMs (depleted using clodronate-filled liposomes) (Fig. 4k,l). Despite no observable drop in the proportion of pericytes within the tumor over the short-term acute treatment

6

regimen (Fig. 4m), proliferation of the pericyte population was significantly diminished in the absence of CD206^{hi}MHCII^{lo}Lyve-1^{+} PvTAMs, with no change in the proportion of cells which had incorporated Edu^{+} cells within the CD34^{+} CAF or tumor cell compartments (Fig. 4n). Pericytes are important to angiogenesis, supporting vessel stabilization and endothelial cell survival [37]. The endothelium's expression of PDGF-β which signals on PDGF-Rβ expressed on pericytes has been demonstrated as a vital chemo-attractant axis for localizing pericyte progenitors to the vasculature [54] [55, 56, 57]. In the absence of pericytes, as is observed in *Pdgfb* and *Pdgfrb* knockout mice, the vasculature displays systemic defects [58]. Our data suggest that despite endothelial cells playing a well-established role in maintaining pericytes in the perivascular space [55, 56], the role of directing expansion of this population during pathological angiogenesis is divested to the immune system, specifically the CD206^{hi}MHCII^{lo}Lyve-1^{+} PvTAMs.

To unravel the underlying mechanism for how CD206^{hi}MHCII^{lo}Lyve-1^{+} PvTAMs were orchestrating pericyte expansion, we utilized *CellPhoneDB*, a manually curated repository and computational framework to map the possible biological ligand:receptor interactions within RNA-seq datasets [59] between the CD206^{hi}MHCII^{lo}Lyve-1^{+} PvTAMs, pericytes and CD31^{+} endothelial cells (which were bulk-population RNA-sequenced) to construct an interactome of the major cell types in the perivascular niche (Fig. 5a). There were a total of 788 possible unique interactions between these three cell types, highlighting the range of potential crosstalk between these populations in constructing the angiogenic niche (Supplementary Fig. 5a). To refine this list, we selected for non-integrin mediated ligands which were enriched in CD206^{hi}MHCII^{lo}Lyve-1^{+} PvTAMs compared to other TAM populations and could interact with receptors specifically expressed on pericytes and not endothelial cells (Fig. 5b,c). This highlighted the selective expression of *Pdgfc* [60] by the CD206^{hi}MHCII^{lo}Lyve-1^{+} PvTAMs which could signal through *Pdgfra* expressed selectively on the pericytes (Fig. 5c). More broadly, the CD206^{hi}MHCII^{lo}Lyve-1^{+} TAM subset was a major source of *Pdgfc* in the tumor (Fig. 5d and Supplementary Fig. 5b).

PDGFRs form either homo- or hetero-dimers between the α and β receptor subunit (αα, αβ and ββ) and a homodimer of PDGF-C (PDGF-CC) selectively signals through PDGFRα [61] which has been demonstrated to be a mitogenic and migratory factor for human dermal fibroblasts [62, 63]. PDGF-CC is a prognostic factor for poor survival in breast cancer [64] and has been demonstrated to be important to angiogenesis [65, 66]. The bulk population RNA-seq demonstrated that pericytes selectively expressed *Pdgfra* (Fig. 5e), and the protein was also detectable (Fig. 5f), emphasizing the selectivity of the PDGF-CC:PDGFRα axis within the perivascular niche. Tumors grow slower in *MMTV-PyMT Pdfgc*^{-/-} mice and display increased necrotic areas and evidence of hemorrhage [64]. To assess whether PDGF-CC may play a

7

role in directing the proliferation of the pericyte population within the perivascular niche we administered neutralizing antibodies to PDGF-CC, within an acute treatment regimen, in tumor bearing *MMTV-PyMT* mice (Fig. 5g). Neutralization of PDGF-CC did not affect the abundance of the cell populations at the acute timepoint (Fig. 5h) but did diminish Edu$^+$ incorporation selectively of the pericytes, but not in the tumor or CD45$^-$CD31$^+$ endothelial cells (Fig. 5i). This highlighted that the expansion of pericytes was PDGF-CC dependent and could account for the role of CD206^{hi}MHCII^{lo}Lyve-1$^+$ PvTAMs in expanding the pericyte population to support angiogenesis in cancer. In accordance with our observations in murine models, using The Cancer Genome Atlas (TCGA) we revealed an enrichment for a SMA$^+$ pericyte signature (using genes identified in the murine population) above that of healthy tissue in human breast cancer (Supplementary Fig. 5c) and interestingly the SMA$^+$ pericyte signature also positively correlated with *PDGFC* expression within the tumor (Supplementary Fig. 5d).

This study characterizes a biologically important subset of TAMs selectively expressing Lyve-1 that are associated with angiogenesis through a mechanism independent of VEGF. We demonstrate that the Lyve-1$^+$ PvTAM subset, which only accounts for 1.4±0.4% of live tumoral cells, is pivotal to tumor growth. We define a new role for PvTAMs in directing the expansion of the pericyte population to support angiogenesis and disease progression, orchestrated through their expression of PDGF-CC (Fig. 5j). This study further supports PvTAMs as a therapeutic target in cancer and highlights PDGF-CC as a non-redundant effector molecule facilitating their pro-tumoral properties.

Acknowledgements

Biomedical Sciences. PyMT x Kaede studies were supported by a Cancer Immunology Project Award (C54019/A27535) from Cancer Research UK awarded to D.R.W. The research was supported by the Cancer Research UK King's Health Partners Centre and Experimental Cancer Medicine Centre at King's College London, and the National Institute for Health Research (NIHR) Biomedical Research Centre based at Guy's and St Thomas' NHS Foundation Trust and King's College London. The views expressed are those of the authors and not necessarily those of the NHS, the NIHR or the Department of Health.

Competing interests

Authors declare no competing interests relating to this work.

Author contributions

J.W.O., J.N.A. conceived the project, designed the approach, performed experiments, interpreted the data wrote the manuscript. J.E.A., I.D., E.J.H., I.B., J.C., T.M., P.G., R.N. designed the approach, performed experiments, and interpreted the data. S.E.P., T.N., F.D., S.K., D.R.W., T.L. designed experiments, interpreted the data and provided key expertise.

Online Methods

Mice

MMTV-PyMT (*PyMT*) mice used in this study were on an FVB/N background. Balb/c and C57Bl/6 wild type mice were obtained from Charles River. Female C57Bl/6 homozygous *Kaede* mice [47] were crossed with male *MMTV-PyMT* (FVB background) mice and the F1 offspring used experimentally. Cohort sizes were informed by prior studies [1, 6, 40, 67]. All mice used for experiments were female and randomly assigned to treatment groups. Mice were approximately 21-26 g when tumors became palpable. Experiments were performed in at least duplicate and for spontaneous *MMTV-PyMT* tumor studies individual mice were collected on separate days and all data points are presented.

Tumor studies

Murine 4T1 mammary adenocarcinoma, Lewis lung carcinoma (LL2) and B16-F10 melanoma cells were obtained from ATCC. 2.5×10^5 cells in 100µl RPMI and were injected by subcutaneous (s.c.) injection into the mammary fat pad of syngeneic Balb/c (4T1) or

9

C57Bl/6 (B16-F10 and LL2) female mice that were six to eight weeks of age. In studies using *MMTV-PyMT* mice tumors arose spontaneously. When tumors became palpable, volumes were measured every 2 days using digital caliper measurements of the long (L) and short (S) dimensions of the tumor. Tumor volume was established using the following equation: Volume= $(S^2 \text{x} L)/2$. *PyMT/Kaede* mice were photo-labelled under anesthesia, individual tumors mice were exposed to a violet light (405nm wavelength) through the skin for nine 20 second exposure cycles with a short 5 second break interval between each cycle. Black cardboard was used to shield the rest of the mouse throughout the photoconversion procedure. Mice for 0 h time points were culled immediately after photoconversion. This photoconversion approach was adapted from that used to label peripheral lymph nodes [68]. Tumor tissue for flow cytometry analyses were enzyme-digested to release single cells as previously described [40]. In brief, tissues were minced using scalpels, and then single cells were liberated by incubation for 60 mins at 37°C with 1 mg/ml Collagenase I from *Clostridium Histolyticum* (Sigma-Aldrich) and 0.1 mg/ml Deoxyribonuclease I (AppliChem) in RPMI (Gibco). Released cells were then passed through a 70 µm cell strainer prior to staining for flow cytometry analyses. Viable cells were numerated using a hemocytometer with trypan blue (Sigma-Aldrich) exclusion. For drug treatments, drugs were freshly prepared on the day of injection and administered by intraperitoneal (i.p.) injection using a 26 G needle. For EdU experiments mice were injected i.p. with 50 mg/kg EdU dissolved in Dulbecco's phosphate buffered saline (PBS) and sacrificed 4 hours post-injection. To liposome deplete Pv macrophages, *MMTV-PyMT* mice were injected i.p. with 150 µl of either clodronate- or PBS-filled liposomes (Anionic Clophosome, FormuMax) on the indicated days. To label PvTAM, *MMTV-PyMT* mice were injected i.p. with 150 µl of DiI fluorescent tracing liposomes (Anionic Clophosome, Formumax). To neutralize PDGF-CC, mice were injected i.p. with 100 µg of a goat anti-PDGF-C neutralizing antibody (AF1447, Bio-techne) solubilized in PBS on day -2 and -1 prior to analysis.

Murine Tissue Staining

Mouse mammary tumors were fixed overnight (O.N.) in 4% paraformaldehyde, followed by O.N. dehydration in 30% sucrose prior to embedding in OCT and snap freezing in liquid nitrogen. Frozen sections from these tumors were fixed in 4% paraformaldehyde in PBS for 10 mins at RT and were washed in Tris Buffered Saline (100mM Tris, 140mM NaCl), 0.05%, Tween 20, pH7.4 (TBST) and blocked with TBST, 10% donkey serum (Sigma-Aldrich), 0.2% Triton X-100. Immunofluorescence was performed as previously described [1]. The following antibodies and dilutions were used: F4/80 1:100 (C1:A3-1, Bio-RAD), αSMA 1:100 (AS-

29553, Anaspec), CD31 1:100 (MEC13.1, Biolegend), CD31 1:100 (ab28364 Abcam), mKi67 1:100 (AF649 R&D), CD34 1:100 (RAM34, Invitrogen), Desmin 1:100 (PA5-19063, Invitrogen). Primary antibodies were detected using antigen specific Donkey IgG, used at 1:200: AlexaFluor® 488 anti-rabbit IgG, AlexaFluor® 488 anti-rat IgG, AlexaFluor® 568 anti-rabbit IgG, AlexaFluor® 568 anti-goat IgG, AlexaFluor® 647 anti-rabbit IgG (Thermo Fisher Scientific). NL657 anti-rat goat IgG (R&D) and Cy3 anti-sheep donkey IgG (Jackson Immuno) were also used. Viable blood vessels were visualized in mice through i.v. injection of FITC-conjugated dextran (MW20,000, Thermo Fisher Scientific) 20 min prior to sacrifice. Nuclei were stained using 1.25 µg/ml 4',6-diamidino-2-phenylindole,dihydrochloride (DAPI) (Thermo Fisher Scientific). Images were acquired using a Nikon Eclipse Ti-E Inverted spinning disk confocal with associated NIS Elements software. Quantitative data was acquired from the images using NIS Elements software.

Human Tissue Staining

FFPE human breast adenocarcinoma tissue sections of 4 µm were incubated at 60°C for 1 h, before being deparaffinized with Tissue-Tek® DRS™2000, Sakura. Heat-induced antigen retrieval was performed using a pressure cooker (MenaPath Access Retrieval Unit, PASCAL). The slides were immersed in modified citrate buffer pH 6 and gradually heated to 125°C. Excess of antigen retrieval buffer was washed firstly with distilled water followed by PBS, before incubation of the slides in blocking buffer containing 0.5% Triton and 5% donkey serum (Sigma) for 30 mins at room temperature. The sections were then probed with anti-CD68 1:100 (KP1, Invitrogen), anti-αSMA 1:200 (1A4, Sigma-Aldrich) and anti-CD31 1:100 (EP3095, Abcam) diluted in blocking buffer overnight at 4°C. After further washing, sections were stained for 2 h with donkey IgG antibodies purchased from Jackson Immunoresearch and used at 1:600; AlexaFluor® 647 anti-mouse IgG and AlexaFluor® 488 anti-rabbit IgG. After washing in PBS, the sections were incubated with anti-αSMA conjugated with CY3 probe 1:200 (1A4, Sigma-Aldrich). Counterstaining was performed with 1:2000 DAPI (Cell Signalling Technology) for 5 mins, followed by a wash step using PBS. Mounting medium (Fluorsave, Millipore) was applied to the slides. Images were acquired using a Nikon Eclipse Ti-E Inverted spinning disk confocal with associated NIS Elements software.

Flow cytometry

Flow cytometry was performed as previously described [6]. The following antibodies against the indicated antigen were purchased from Thermo Fisher Scientific and were used at 1 µg/ml unless stated otherwise: CD3ε APC and PE (145-2C11), CD4 FITC (RM4-5), CD8β eFluor®450 (H35-17.2), CD11b APC (M1/70), CD11c APC-eFluor®780 (N418), CD16/32 (2.4G2; Tonbo Biosciences), CD19 BV421 (6D5; Biolegend®), CD29 APC (eBioHMb1-1), CD31 eFluor® 450 and PE (390), CD34 FITC and APC (RAM34), CD45 APC-eFluor® 780, FITC and PerCP-Cy5.5 (30-F11), CD90.2 eFluor® 450 (53-2.1), CD90.1 eFluor® 450 (HIS51), CD90.1 BV510 (OX-7), CD103 PE (2E7), CD206 APC (FAB2535A; Bio-Techne), F4/80 PE (BM8; Biolegend®), F4/80 BV421 (BM8; Biolegend®), FAP (10 µg/ml, AF3715, Bio-Techne), Ly6C PE and eFluor® 450 (HK1.4), Ly6G FITC (1A8; Biolegend®), Lyve-1 AlexaFluor® 488 (ALY7), MHCII PE and FITC (M5/114.15.2), NK1.1 APC (PK136), PDGFRα PerCP-Cy5.5 (APA5), Ly6A/E AlexaFluor® 700 (D7). Where stated, the following corresponding isotype control antibodies at equivalent concentrations to that of the test stain were used: Armenian Hamster IgG APC (eBio299Arm), goat IgG APC and PE (Bio-techne), rat IgG2a APC, PE and FITC (eBR2a) and rat IgG2b APC and eFluor® 450 (eB149/10H5). Intracellular stains were performed as previously described [6]. Dead cells and red blood cells were excluded using 1 µg/ml 7-amino actinomycin D (7AAD; Sigma-Aldrich), Fixable Viability Dye eFluor® 780 (Invitrogen) or DAPI alongside anti-Ter-119 PerCP-Cy5.5 or APC-eFluor® 780 (Ter-119; Invitrogen). The FAP primary antibody was detected with a secondary biotin-conjugated anti-goat/sheep mouse IgG and 1:1000 Streptavidin PE-Cy7 (Thermo Fisher Scientific). EdU was detected using the Click-IT Plus Flow Cytometry Assay with AlexaFluor® 488 (Thermo Fisher Scientific) in accordance with the manufacturers' specifications. Briefly, cells were stained with cell surface antibodies and then fixed and permeabilized and the click chemistry reaction was performed as specified with AF488-conjugated Picolyl Azide to identify EdU incorporated into the genomic DNA. Cells were sorted to acquire pure populations using a FACSAria (BD Biosciences). Data were collected on a BD FACS Canto II (BD Biosciences) or a BD LSR Fortessa (BD biosciences). Data was analyzed using FlowJo software (BD biosciences). Unsupervised clustering of flow cytometry data was performed using the ImmunoCluster package [69] . Briefly, the single-cell data was asinh transformed with cofactor of 150 and clustering was performed with and ensemble method using FlowSOM [44] and ConsensusClusterPlus [70] to k=8 clusters, based on the elbow criterion, which were manually merged based on expression profiles into biologically meaningful populations as previously outlined [71]. Dimensionality reduction for visualization purposes was performed with UMAP [22].

Quantitative real time quantitative PCR

12

mRNA was extracted from FACS-sorted cell populations using the Trizol method and converted to cDNA/amplified using the CellAmp™ Whole Transcriptome Amplification Kit (Real Time), Ver. 2 kit (Takara) according to the manufacturer's protocol. mRNA of interest was measured using the SuperScriptTM III PlatinumTM One-Step qRT-PCR Kit (Thermo Fisher Scientific) according to the manufacturer's protocol with the primers/probes *Actb Mm02619580_g1* and *Pdgfc* Mm00480295_m1 (Thermo Fisher Scientific). Expression is represented relative to the housekeeping gene *Actb*. Gene expression was measured using an ABI 7900HT Fast Real Time PCR instrument (Thermo Fisher Scientific).

Single-cell RNA-sequencing

TAMs (CD45$^+$Ly6G$^-$CD11b$^+$F4/80^{hi}) were sorted from enzyme-digested *MMTV-PyMT* tumors and a total of 10,502 TAMs were sequenced from three *MMTV-PyMT* tumors and run through the 10x Genomics Chromium platform. An average of 43k reads per cell, a median of 2,400 genes and median UMI count of 9,491 per cells was obtained. Single-cell suspensions were prepared as outlined in the 10x Genomics Single Cell 3' V3 Reagent kit user guide (10x Genomics). Briefly, samples were washed with PBS (Gibco) with 0.04% bovine serum albumin (Sigma-Aldrich) and resuspended in 1 ml PBS, 0.04% BSA. Sample viability was assessed using trypan blue (Thermo Fisher Scientific) exclusion and an EVE automated cell counter (Alphametrix) in duplicate, in order to determine the appropriate volume for each sample to load into the Chromium instrument. The sorted TAMs were loaded onto a Chromium Instrument (10x Genomics) to generate single-cell barcoded droplets according to the manufacturers' protocol using the 10x Genomics Single Cell 3' V3 chemistry. cDNA libraries were prepared as outlined by the Single Cell 3′ Reagent kit v3 user guide and each of the three resulting libraries were sequenced on one lane each of a HiSeq 2500 (Illumina) in rapid mode.

Single-cell RNA-sequencing data processing and analysis

The raw sequenced data was processed with the Cell Ranger analysis pipeline version 3.0.2 by 10x Genomics (http://10xgenomics.com/). Briefly, sequencing reads were aligned to the mouse transcriptome mm10 using the STAR aligner [72]. Subsequently, cell barcodes and unique molecular identifiers underwent Cell Ranger filtering and correction. Reads associated with the retained barcodes were quantified and used to build a transcript count tables for each sample. Downstream analysis was performed using the Seurat v3 R package [73]. Before analysis, we first performed quality control filtering with the following parameters: cells were discarded on the following criteria: where fewer than 800 unique genes detected,

reads composed greater than 12% mitochondrial-associated gene transcripts and cells whose number of reads detected per cell was greater than 65k for sample 1 and 2, 60k for sample 3. All genes that were not detected in at least ten single cells were excluded. Based on these criteria the final dataset contained 9,615 TAMs with 25,142 detected genes. The data was first normalized using the LogNormalize function and a scale factor of 10,000. The 2,000 genes with highest variance were selected with the FindVariableGenes function. In order to minimize the effect of cell cycle associated genes in the dimensionality reduction and clustering, cell cycle associated genes defined by the GO term 'Cell Cycle' were removed from the variable gene dataset resulting in 1,765 variable genes. Principal component (PC) analysis was used on the highly variable genes to reduce the dimensionality of the feature space and 35 significant PCs were selected for downstream analysis. To reduce biases caused by technical variation, sequencing depth and capture efficiency, the three sequencing samples were integrated using the Seurat integration method [73] as specified. Clusters were identified by a graph based SNN clustering approach within Seurat using the resolution parameters 0-1 in steps of 0.1, followed by analysis using the Clustree R package [74]. Finally, we used resolution parameter of 0.4 to define 10 clusters. Differentially expressed genes were identified using the FindAllMarkers function where the genes must be detected in a minimum of 25% of cells and have a logFC threshold of 0.25. After identifying marker genes, we excluded two clusters which contained suspected contaminating epithelial cells (enriched in *Epcam*, *Krt18*, *Krt8*) and dying low-quality cells (enriched in mitochondrial genes and ribosomal subunit genes). Ultimately, we identified 8 relevant clusters. We used the Slingshot R package [23] to investigate inferred developmental trajectories in our TAM population. Briefly, dimensionality reduction was performed using diffusion maps with the Destiny R package [75] using the significant PCA principal components used for clustering. A lineage trajectory was mapped into the diffusion space using the first 15 diffusion components (DCs) by Slingshot and each cell was assigned a pseudotime value based on its predicted position along the predicted trajectories. We selected the cluster TAM01 as the base state for the trajectory because it had the lowest M1/M2 activation-associated gene score amongst the terminal trajectory branch clusters, no discriminating upregulated GO pathways and the fewest differentially expressed genes and represented the most naïve TAM transcriptomic base state. To detect non-linear patterns in gene expression over pseudotime trajectory, we used the top variable gene set and regressed each gene on the pseudotime variable we generated, using a general additive model (GAM) with the GAM R package[76]. Heatmaps were generated with the ComplexHeatmap package [50].

Bulk RNA-sequencing

Cells were sorted directly into RLT plus buffer (Qiagen) supplemented with 2-β-mercaptoethanol (BME) (Gibco) and lysates were immediately stored at -80°C until used. RNA was extracted with the RNeasy Plus Micro kit (Qiagen) as per the manufacturers' protocol, in addition to on-column DNase digestions specified by the manufacturer (Qiagen). cDNA was generated and amplified using the SMARTseq v4 Ultra Low Input RNA Kit (Clontech) on the contactless Labcyte liquid handling system (Beckman Coulter Life Sciences). Two hundred ng of amplified cDNA was used from each sample where possible to generate libraries using the Ovation Ultralow Library System V2 kit (NuGEN). In brief, cDNA was fragmented through sonication on Covaris E220 (Covaris Inc.), repaired, and polished followed by ligation of indexed adapters. Adapter-ligated cDNA was pooled before final amplification to add flow cell primers. Libraries were sequenced on HiSeq 2500 (Illumina) for 100 paired-end cycles in rapid mode.

Bulk RNA-sequencing data processing and analysis

Pre-alignment QC for each sample, independently for forward and reverse reads, was performed using the standalone tool FastQC. Reads were trimmed using Trimmomatic [77] and aligned to the reference genome (mm10) using HISAT2 [78]. PCR duplicates were removed using SAMtools[79]. Counts were generated using the GenomicAlignment [80] package using mm10. Prior to performing differential gene expression analysis, genes with very low expression were discarded. Differential expression analysis was performed with DESeq2 [81] package in R. The test statistics' p-values were adjusted for multiple testing using the procedure of Benjamini and Hochberg. Genes with adjusted p-values lower than 0.05 and absolute log2 fold change greater than 1 were considered significant.

Gene Ontology pathway enrichment analysis

Enriched pathways were identified based on differentially expressed genes using gProfiler[82] (http://www.biit.cs.ut.ee/gprofiler/). We used pathways gene sets from the 'biological processes' (GO:BP) of Gene Ontology (http://www.geneontology.org/). All p-values were adjusted for multiple testing using the procedure of Benjamini and Hochberg.

Ligand:receptor mapping analysis

Ligand:receptor mapping was performed with the local python implementation of the CellPhoneDB v2.0 tool (https://github.com/Teichlab/cellphonedb) [83] run without the statistical method. Cell type ligand receptome data was generated with scRNA-seq TAM06 differentially expressed genes and CD34⁻ CAF1 and endothelial cells bulk-sequencing data as input, selecting genes with expression of 16 normalized counts or greater as input. The resulting interaction list was filtered on the ligand:receptor pairs selecting for ligands present in the GO term 'growth factor activity' that were investigated further as potential candidates.

Computational analysis of cancer patient data

RSEM normalized expression datasets from the Cancer Genome Atlas (TCGA) were downloaded from the Broad Institute Firehose resource (https://gdac.broadinstitute.org/) and analyzed using custom R scripts. The CAF1 gene expression signature was generated by taking the mean normalized log2-transformed expression value of the component signature genes. The CAF1 gene signature genes were selected from the top 25 differentially expressed Pericyte (CAF1) genes by Log Fold change as the maximum set for which a significant positive correlation was observed between all genes and *ACTA2* (αSMA). The final gene set was as follows: *ACTA2, MMP13, LRRC15, COL10A1, SPON1, COL1A1*.

Statistics

Normality and homogeneity of variance were determined using a Shapiro-Wilk normality test and an F-test respectively. Statistical significance was then determined using a two-sided unpaired Students *t* test for parametric, or Mann-Whitney test for nonparametric data using GraphPad Prism 8 software. A Welch's correction was applied when comparing groups with unequal variances. Statistical analysis of tumor growth curves was performed using the "compareGrowthCurves" function of the statmod software package [84]. No outliers were excluded from any data presented.

Study approval

All experiments involving animals were approved by the Animal and Welfare and Ethical Review Boards of King's College London and the University of Birmingham, and the Home Office UK. Human breast adenocarcinoma tissue was obtained with informed consent under

ethical approval from the King's Health Partners Cancer Biobank (REC reference 12/EE/0493).

Data Availability

The transcriptomic datasets that support the findings of this study will be publicly available. The authors declare that all other data supporting the findings of this study are available within the paper and its supplementary information files.

<u>References</u>

1. Muliaditan, T. *et al.* Macrophages are exploited from an innate wound healing response to facilitate cancer metastasis. *Nature communications* **9**, 2951 (2018).

2. Cassetta, L. *et al.* Human Tumor-Associated Macrophage and Monocyte Transcriptional Landscapes Reveal Cancer-Specific Reprogramming, Biomarkers, and Therapeutic Targets. *Cancer cell* **35**, 588-602 e510 (2019).

3. Noy, R. & Pollard, J.W. Tumor-Associated Macrophages: From Mechanisms to Therapy. *Immunity* **41**, 49-61 (2014).

4. De Palma, M. *et al.* Tie2 identifies a hematopoietic lineage of proangiogenic monocytes required for tumor vessel formation and a mesenchymal population of pericyte progenitors. *Cancer cell* **8**, 211-226 (2005).

5. Lin, E.Y. *et al.* Vascular endothelial growth factor restores delayed tumor progression in tumors depleted of macrophages. *Mol Oncol* **1**, 288-302 (2007).

6. Arnold, J.N., Magiera, L., Kraman, M. & Fearon, D.T. Tumoral immune suppression by macrophages expressing fibroblast activation protein-alpha and heme oxygenase-1. *Cancer immunology research* **2**, 121-126 (2014).

7. Etzerodt, A. *et al.* Specific targeting of CD163(+) TAMs mobilizes inflammatory monocytes and promotes T cell-mediated tumor regression. *The Journal of experimental medicine* **216**, 2394-2411 (2019).

8. DeNardo, D.G. *et al.* Leukocyte Complexity Predicts Breast Cancer Survival and Functionally Regulates Response to Chemotherapy. *Cancer discovery* **1**, 54-67 (2011).

9. Mitchem, J.B. *et al.* Targeting tumor-infiltrating macrophages decreases tumor-initiating cells, relieves immunosuppression, and improves chemotherapeutic responses. *Cancer research* **73**, 1128-1141 (2013).

10.   Muliaditan, T. *et al.* Repurposing tin mesoporphyrin as an immune checkpoint inhibitor shows therapeutic efficacy in preclinical models of cancer. *Clinical cancer research : an official journal of the American Association for Cancer Research* (2018).

11.   DeNardo, D.G. *et al.* CD4(+) T cells regulate pulmonary metastasis of mammary carcinomas by enhancing protumor properties of macrophages. *Cancer cell* **16**, 91-102 (2009).

12.   Qian, B.Z. *et al.* CCL2 recruits inflammatory monocytes to facilitate breast-tumour metastasis. *Nature* **475**, 222-225 (2011).

13.   Arwert, E.N. *et al.* A Unidirectional Transition from Migratory to Perivascular Macrophage Is Required for Tumor Cell Intravasation. *Cell reports* **23**, 1239-1248 (2018).

14.   Wyckoff, J.B. *et al.* Direct visualization of macrophage-assisted tumor cell intravasation in mammary tumors. *Cancer research* **67**, 2649-2656 (2007).

15.   Harney, A.S. *et al.* Real-Time Imaging Reveals Local, Transient Vascular Permeability, and Tumor Cell Intravasation Stimulated by TIE2hi Macrophage-Derived VEGFA. *Cancer discovery* **5**, 932-943 (2015).

16.   Murray, P.J. *et al.* Macrophage activation and polarization: nomenclature and experimental guidelines. *Immunity* **41**, 14-20 (2014).

17.   Zhang, L. *et al.* Single-Cell Analyses Inform Mechanisms of Myeloid-Targeted Therapies in Colon Cancer. *Cell* **181**, 442-459 e429 (2020).

18.   Lewis, C.E., Harney, A.S. & Pollard, J.W. The Multifaceted Role of Perivascular Macrophages in Tumors. *Cancer cell* **30**, 365 (2016).

19.   Qian, B. *et al.* A distinct macrophage population mediates metastatic breast cancer cell extravasation, establishment and growth. *PloS one* **4**, e6562 (2009).

20.   Friebel, E. *et al.* Single-Cell Mapping of Human Brain Cancer Reveals Tumor-Specific Instruction of Tissue-Invading Leukocytes. *Cell* **181**, 1626-1642 e1620 (2020).

21.   Guy, C.T., Cardiff, R.D. & Muller, W.J. Induction of mammary tumors by expression of polyomavirus middle T oncogene: a transgenic mouse model for metastatic disease. *Molecular and cellular biology* **12**, 954-961 (1992).

22.   Becht, E. *et al.* Dimensionality reduction for visualizing single-cell data using UMAP. *Nature biotechnology* (2018).

23.   Street, K. *et al.* Slingshot: cell lineage and pseudotime inference for single-cell transcriptomics. *BMC genomics* **19**, 477 (2018).

24.   Mills, C.D., Kincaid, K., Alt, J.M., Heilman, M.J. & Hill, A.M. M-1/M-2 macrophages and the Th1/Th2 paradigm. *Journal of immunology* **164**, 6166-6173 (2000).

25.   Orecchioni, M., Ghosheh, Y., Pramod, A.B. & Ley, K. Macrophage Polarization: Different Gene Signatures in M1(LPS+) vs. Classically and M2(LPS-) vs. Alternatively Activated Macrophages. *Frontiers in immunology* **10**, 1084 (2019).

26.   Boskovic, J. *et al.* Structural model for the mannose receptor family uncovered by electron microscopy of Endo180 and the mannose receptor. *The Journal of biological chemistry* **281**, 8780-8787 (2006).

27.   Jackson, D.G., Prevo, R., Clasper, S. & Banerji, S. LYVE-1, the lymphatic system and tumor lymphangiogenesis. *Trends in immunology* **22**, 317-321 (2001).

28.   Ensan, S. *et al.* Self-renewing resident arterial macrophages arise from embryonic CX3CR1(+) precursors and circulating monocytes immediately after birth. *Nature immunology* **17**, 159-168 (2016).

29.   Cho, C.H. *et al.* Angiogenic role of LYVE-1-positive macrophages in adipose tissue. *Circulation research* **100**, e47-57 (2007).

30.   Pinto, A.R. *et al.* An abundant tissue macrophage population in the adult murine heart with a distinct alternatively-activated macrophage profile. *PloS one* **7**, e36814 (2012).

31.   Xu, H., Chen, M., Reid, D.M. & Forrester, J.V. LYVE-1-positive macrophages are present in normal murine eyes. *Investigative ophthalmology & visual science* **48**, 2162-2171 (2007).

32.   Chakarov, S. *et al.* Two distinct interstitial macrophage populations coexist across tissues in specific subtissular niches. *Science* **363** (2019).

33.   Dollt, C. *et al.* The shedded ectodomain of Lyve-1 expressed on M2-like tumor-associated macrophages inhibits melanoma cell proliferation. *Oncotarget* **8**, 103682-103692 (2017).

34.   Buiting, A.M., Zhou, F., Bakker, J.A., van Rooijen, N. & Huang, L. Biodistribution of clodronate and liposomes used in the liposome mediated macrophage 'suicide' approach. *Journal of immunological methods* **192**, 55-62 (1996).

35.   Spranger, S., Dai, D., Horton, B. & Gajewski, T.F. Tumor-Residing Batf3 Dendritic Cells Are Required for Effector T Cell Trafficking and Adoptive T Cell Therapy. *Cancer cell* **31**, 711-723 e714 (2017).

36.   Roberts, E.W. *et al.* Critical Role for CD103(+)/CD141(+) Dendritic Cells Bearing CCR7 for Tumor Antigen Trafficking and Priming of T Cell Immunity in Melanoma. *Cancer cell* **30**, 324-336 (2016).

37.   De Palma, M., Biziato, D. & Petrova, T.V. Microenvironmental regulation of tumour angiogenesis. *Nature reviews. Cancer* **17**, 457-474 (2017).

38.   Folkman, J. Tumor angiogenesis: therapeutic implications. *The New England journal of medicine* **285**, 1182-1186 (1971).

39.   Hall, S.E., Savill, J.S., Henson, P.M. & Haslett, C. Apoptotic neutrophils are phagocytosed by fibroblasts with participation of the fibroblast vitronectin receptor and involvement of a mannose/fucose-specific lectin. *Journal of immunology* **153**, 3218-3227 (1994).

40.   Kraman, M. *et al.* Suppression of antitumor immunity by stromal cells expressing fibroblast activation protein-alpha. *Science* **330**, 827-830 (2010).

41.   Bartoschek, M. *et al.* Spatially and functionally distinct subclasses of breast cancer-associated fibroblasts revealed by single cell RNA sequencing. *Nature communications* **9**, 5150 (2018).

42.   Ohlund, D. *et al.* Distinct populations of inflammatory fibroblasts and myofibroblasts in pancreatic cancer. *J Exp Med* **214**, 579-596 (2017).

43.   Costa, A. *et al.* Fibroblast Heterogeneity and Immunosuppressive Environment in Human Breast Cancer. *Cancer Cell* **33**, 463-479 e410 (2018).

44.   Van Gassen, S. *et al.* FlowSOM: Using self-organizing maps for visualization and interpretation of cytometry data. *Cytometry A* **87**, 636-645 (2015).

45.   Armulik, A., Genove, G. & Betsholtz, C. Pericytes: developmental, physiological, and pathological perspectives, problems, and promises. *Developmental cell* **21**, 193-215 (2011).

46.   Sahai, E. *et al.* A framework for advancing our understanding of cancer-associated fibroblasts. *Nature reviews. Cancer* **20**, 174-186 (2020).

47. Tomura, M. *et al.* Monitoring cellular movement in vivo with photoconvertible fluorescence protein "Kaede" transgenic mice. *Proceedings of the National Academy of Sciences of the United States of America* **105**, 10871-10876 (2008).

48. Chimileski, S., Franklin, M.J. & Papke, R.T. Biofilms formed by the archaeon Haloferax volcanii exhibit cellular differentiation and social motility, and facilitate horizontal gene transfer. *BMC biology* **12**, 65 (2014).

49. Franklin, R.A. *et al.* The cellular and molecular origin of tumor-associated macrophages. *Science* **344**, 921-925 (2014).

50. Binnewies, M. *et al.* Unleashing Type-2 Dendritic Cells to Drive Protective Antitumor CD4(+) T Cell Immunity. *Cell* **177**, 556-571 e516 (2019).

51. Miller, I. *et al.* Ki67 is a Graded Rather than a Binary Marker of Proliferation versus Quiescence. *Cell reports* **24**, 1105-1112 e1105 (2018).

52. Stark, K. *et al.* Capillary and arteriolar pericytes attract innate leukocytes exiting through venules and 'instruct' them with pattern-recognition and motility programs. *Nature immunology* **14**, 41-51 (2013).

53. Minutti, C.M. *et al.* A Macrophage-Pericyte Axis Directs Tissue Restoration via Amphiregulin-Induced Transforming Growth Factor Beta Activation. *Immunity* **50**, 645-654 e646 (2019).

54. Lindahl, P., Johansson, B.R., Leveen, P. & Betsholtz, C. Pericyte loss and microaneurysm formation in PDGF-B-deficient mice. *Science* **277**, 242-245 (1997).

55. Bergers, G. & Song, S. The role of pericytes in blood-vessel formation and maintenance. *Neuro-oncology* **7**, 452-464 (2005).

56. Abramsson, A., Lindblom, P. & Betsholtz, C. Endothelial and nonendothelial sources of PDGF-B regulate pericyte recruitment and influence vascular pattern formation in tumors. *The Journal of clinical investigation* **112**, 1142-1151 (2003).

57. Sennino, B. *et al.* Sequential loss of tumor vessel pericytes and endothelial cells after inhibition of platelet-derived growth factor B by selective aptamer AX102. *Cancer research* **67**, 7358-7367 (2007).

58. Hellstrom, M. *et al.* Lack of pericytes leads to endothelial hyperplasia and abnormal vascular morphogenesis. *The Journal of cell biology* **153**, 543-553 (2001).

59. Vento-Tormo, R. *et al.* Single-cell reconstruction of the early maternal-fetal interface in humans. *Nature* **563**, 347-353 (2018).

60.   Li, X. *et al.* PDGF-C is a new protease-activated ligand for the PDGF alpha-receptor. *Nature cell biology* **2**, 302-309 (2000).

61.   Gilbertson, D.G. *et al.* Platelet-derived growth factor C (PDGF-C), a novel growth factor that binds to PDGF alpha and beta receptor. *The Journal of biological chemistry* **276**, 27406-27414 (2001).

62.   Jinnin, M. *et al.* Regulation of fibrogenic/fibrolytic genes by platelet-derived growth factor C, a novel growth factor, in human dermal fibroblasts. *Journal of cellular physiology* **202**, 510-517 (2005).

63.   Shook, B.A. *et al.* Myofibroblast proliferation and heterogeneity are supported by macrophages during skin repair. *Science* **362** (2018).

64.   Roswall, P. *et al.* Microenvironmental control of breast cancer subtype elicited through paracrine platelet-derived growth factor-CC signaling. *Nature medicine* **24**, 463-473 (2018).

65.   Li, X. *et al.* VEGF-independent angiogenic pathways induced by PDGF-C. *Oncotarget* **1**, 309-314 (2010).

66.   Crawford, Y. *et al.* PDGF-C mediates the angiogenic and tumorigenic properties of fibroblasts associated with tumors refractory to anti-VEGF treatment. *Cancer cell* **15**, 21-34 (2009).

67.   Muliaditan, T. *et al.* Repurposing Tin Mesoporphyrin as an Immune Checkpoint Inhibitor Shows Therapeutic Efficacy in Preclinical Models of Cancer. *Clinical cancer research : an official journal of the American Association for Cancer Research* **24**, 1617-1628 (2018).

68.   Dutton, E.E. *et al.* Peripheral lymph nodes contain migratory and resident innate lymphoid cell populations. *Science immunology* **4** (2019).

69.   Opzoomer, J.W. *et al.* ImmunoCluster: A computational framework for the non-specialist to immune profile cellular heterogeneity using liquid and imaging mass, and flow cytometry datasets. *bioRxiv* (2020).

70.   Wilkerson, M.D. & Hayes, D.N. ConsensusClusterPlus: a class discovery tool with confidence assessments and item tracking. *Bioinformatics* **26**, 1572-1573 (2010).

71.   Nowicka, M. *et al.* CyTOF workflow: Differential discovery in high-throughput high-dimensional cytometry datasets. *F1000Research* **6** (2017).

72. Dobin, A. *et al.* STAR: ultrafast universal RNA-seq aligner. *Bioinformatics* **29**, 15-21 (2013).

73. Stuart, T. *et al.* Comprehensive Integration of Single-Cell Data. *Cell* **177**, 1888-1902 e1821 (2019).

74. Zappia, L. & Oshlack, A. Clustering trees: a visualization for evaluating clusterings at multiple resolutions. *Gigascience* **7** (2018).

75. Angerer, P. *et al.* destiny: diffusion maps for large-scale single-cell data in R. *Bioinformatics* **32**, 1241-1243 (2016).

76. Hastie, T.J. & Tibshirani, R.J. *Generalized additive models*, vol. 43. CRC press, 1990.

77. Bolger, A.M., Lohse, M. & Usadel, B. Trimmomatic: a flexible trimmer for Illumina sequence data. *Bioinformatics* **30**, 2114-2120 (2014).

78. Kim, D., Langmead, B. & Salzberg, S.L. HISAT: a fast spliced aligner with low memory requirements. *Nat Methods* **12**, 357-360 (2015).

79. Li, H. *et al.* The Sequence Alignment/Map format and SAMtools. *Bioinformatics* **25**, 2078-2079 (2009).

80. Lawrence, M. *et al.* Software for computing and annotating genomic ranges. *PLoS Comput Biol* **9**, e1003118 (2013).

81. Love, M.I., Huber, W. & Anders, S. Moderated estimation of fold change and dispersion for RNA-seq data with DESeq2. *Genome Biol* **15**, 550 (2014).

82. Raudvere, U. *et al.* g:Profiler: a web server for functional enrichment analysis and conversions of gene lists (2019 update). *Nucleic Acids Res* **47**, W191-W198 (2019).

83. Efremova, M., Vento-Tormo, M., Teichmann, S.A. & Vento-Tormo, R. CellPhoneDB: inferring cell-cell communication from combined expression of multi-subunit ligand-receptor complexes. *Nat Protoc* **15**, 1484-1506 (2020).

84. Elso, C.M. *et al.* Leishmaniasis host response loci (lmr1-3) modify disease severity through a Th1/Th2-independent pathway. *Genes Immun* **5**, 93-100 (2004).
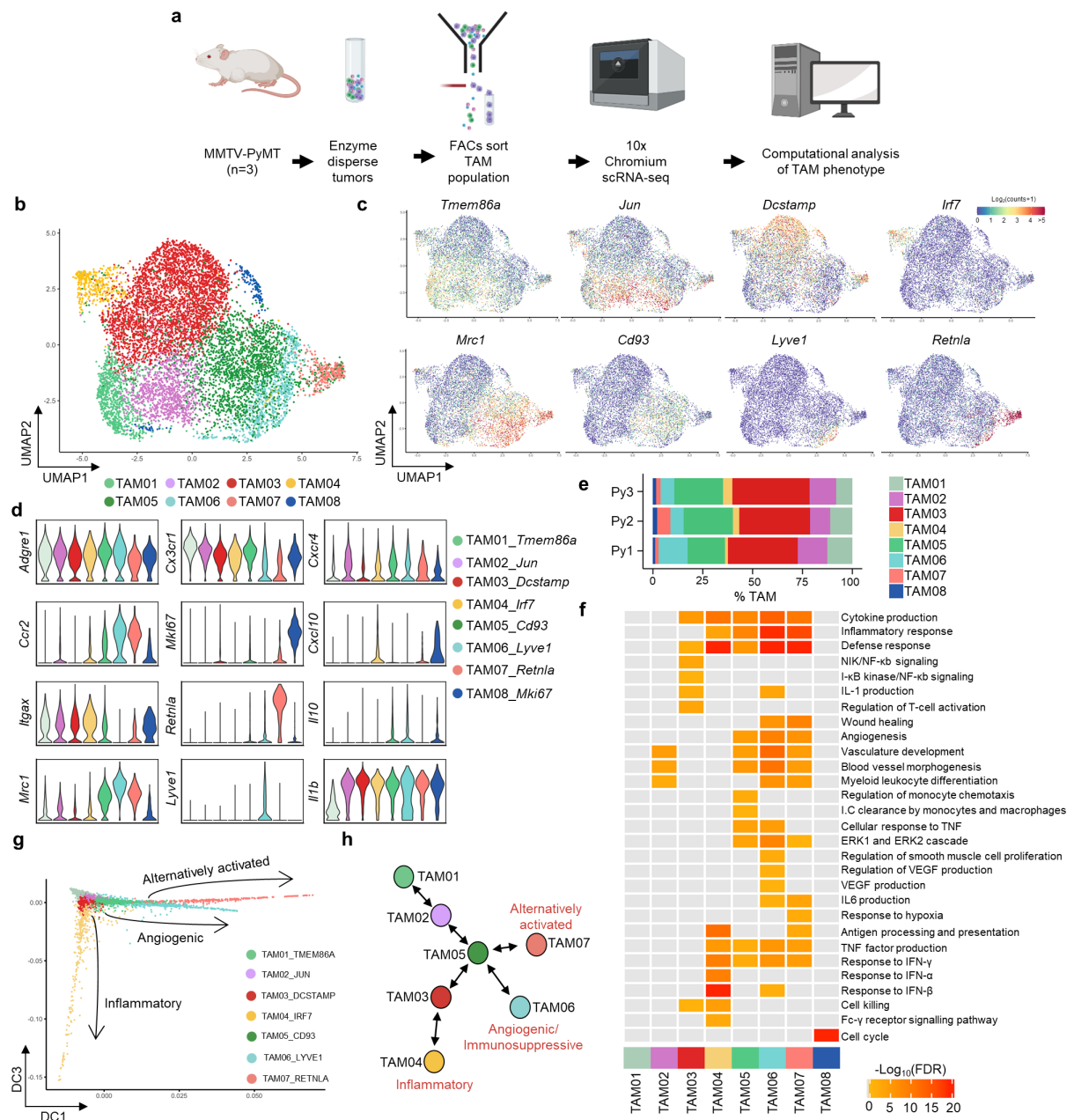
Fig. 1: scRNA-seq of TAMs in *MMTV-PyMT* tumors reveals three distinct polarization pathways. (**a**) Schematic outlining the scRNA-seq experimental workflow which was conducted for n=3 individual *MMTV-PYMT* tumors and mice, sequencing a total of 9,039 cells using the 10X Genomics' Chromium platform. (**b**) UMAP plot of sequenced TAMs colored by their associated cluster identity. (**c**) UMAP visualizations of predicted marker gene expression for distinct TAM clusters shown in (**b**). (**d**) Violin plots of selected genes associated with TAM cluster identity seen in (**b**). (**e**) The relative proportion of each TAM cluster across the individual *MMTV-PyMT* tumors analyzed. (**f**) Heatmap representing significantly upregulated GO pathway terms in one or more TAM clusters. (**g,h**) Scatter plot of single cells projected into two dimensions using diffusion maps, where each cell (dot) is colored by cluster identity, labelled with diffusion component (DC) space annotation representing lineage trajectories predicted by the *Slingshot* package (**g**) and schematic map of each TAM cluster's location along the respective trajectories (**h**).
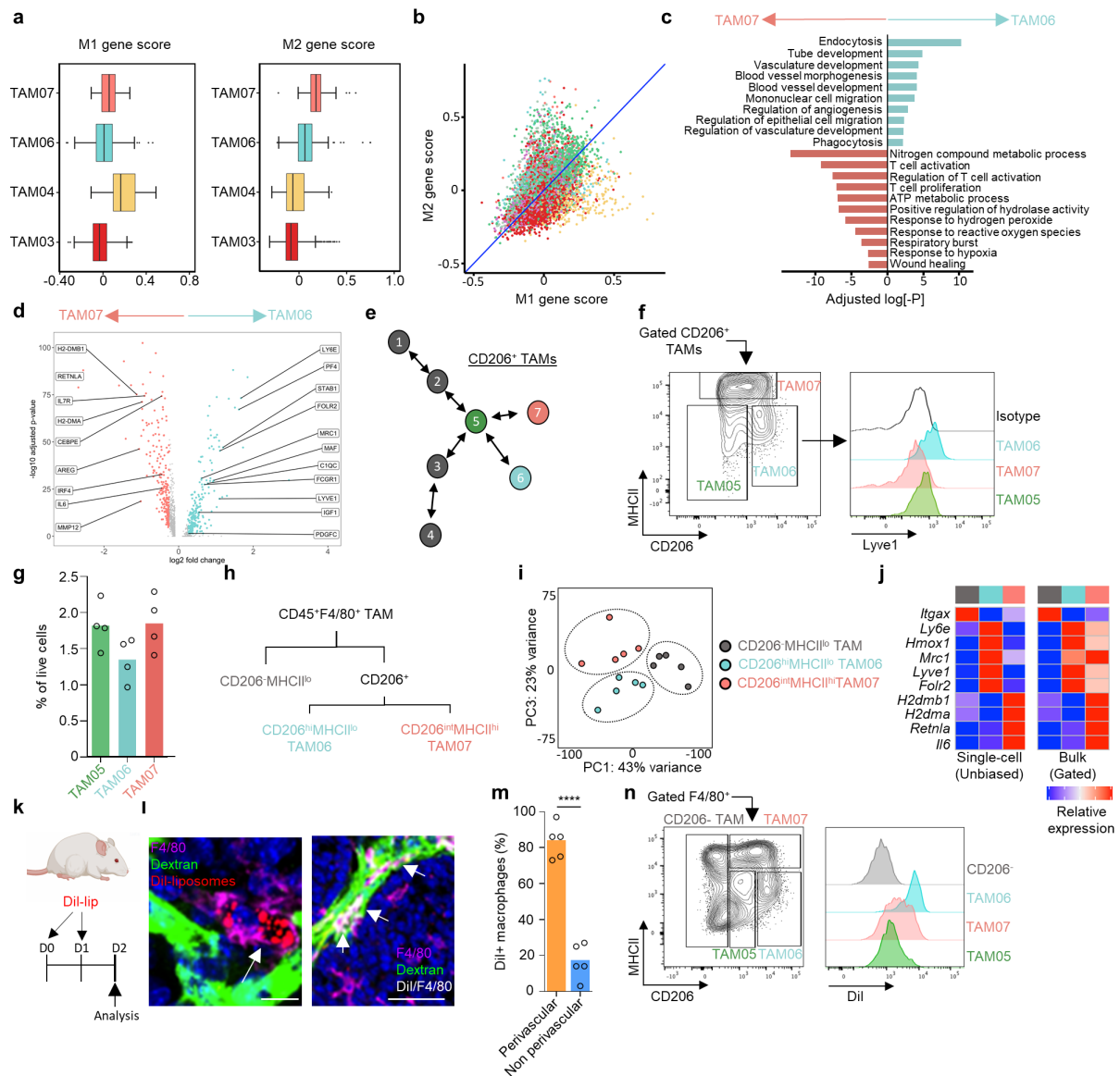
Fig. 2: Lyve-1 marks a pro-tumoral perivascular TAM population. (**a,b**) TAM clusters identified in Fig.1 using scRNA-seq (n=3 mice) were assessed for their similarity to M1/2 macrophage polarization programs. (**a**) Box and whisker plots show normalized mean M1 and M2 associated gene scores across the indicated TAM clusters identified. (**b**) Scatter plot of normalized mean M1/M2 gene score plotted by individual cell (dot) and colored according to their respective TAM cluster. Blue line represents y=x line for reference. (**c,d**) Subset unique, significantly upregulated GO terms based on differentially expressed genes between the two terminal *Mrc1*^high TAM subsets identified in the TAM scRNA-set dataset (**c**), volcano plot showing differentially expressed genes between the two subsets of pro-tumoral TAM (**d**). (**e-g**) Schematic of *Slingshot* trajectory analysis of TAM clusters highlighting predicted *Mrc1* expressing clusters. The clusters where *Mrc1* was not identified as a differentially expressed gene are greyed out (**e**), and mapping of these clusters predicted by the scRNA-seq dataset onto a contour plot of FACs-gated live (7AAD⁻) CD206⁺ F4/80^hi TAMs from enzyme-dispersed *MMTV-PyMT* tumors. TAM populations are separated based on their respective expression of CD206 and MHCII (left panel) and then assessed for their expression of Lyve-1, shown as histograms (right panel; colored shaded histograms) against that of the isotype control staining of F4/80⁺ TAMs (open black line) (**f**) and quantification of the gated populations (**g**). Data representative of n=4 tumors. (**h-j**) Diagram of the FACs gating strategy for TAM populations sorted for bulk RNA-seq (n=5 tumors) (**h**), PCA plot of

the bulk-sequenced TAM populations using the top 2,000 most variable genes (**i**) and heatmaps comparing the relative expression of selected differentially expressed genes for TAM clusters (left), population color is indicative of the populations identified in (h,i) and isolated TAM populations subjected to bulk RNA-seq (right panel), (**j**). (**k-n**) Schematic for experimental approach and dosing strategy to label PvTAMs using Dil-labelled liposomes (**k**). Representative images of frozen sections of *MMTV-PyMT* tumors showing DAPI (nuclei; blue), i.v. dextran marking vasculature (green), Dil from the liposomes (red) and antibody staining against F4/80 (magenta), left shows an example Dil-labelled TAM and right panel shows a larger tumor area displaying co-localizing pixels for Dil and F4/80 as white. White arrows highlight example PvTAM cells which have been labelled by Dil-containing liposomes (**l**) Scale bar 25μm (left panel) and 50μm (right panel). Quantification of the spatial location of Dil$^+$ F4/80$^+$ TAMs relative to vasculature across multiple sections in each tumor across n=5 mice (**m**). Analysis of the TAM population phenotype up-taking Dil-liposomes from enzyme-dispersed tumors within the F4/80^{hi} CD206$^+$ subsets – gate as shown (left) and histogram of the indicated TAM subsets Dil fluorescence (right) (**n**). Box and whisker plots, the boxes show median and upper and lower quartiles and whiskers shows the largest value no more than 1.5*IQR of the respective upper and lower hinges, outliers beyond the end of the whisker are plotted as individual dots. Bar charts represent mean and the dots show individual data points from individual tumors and mice. ** *P*<0.01, *** *P*<0.001.
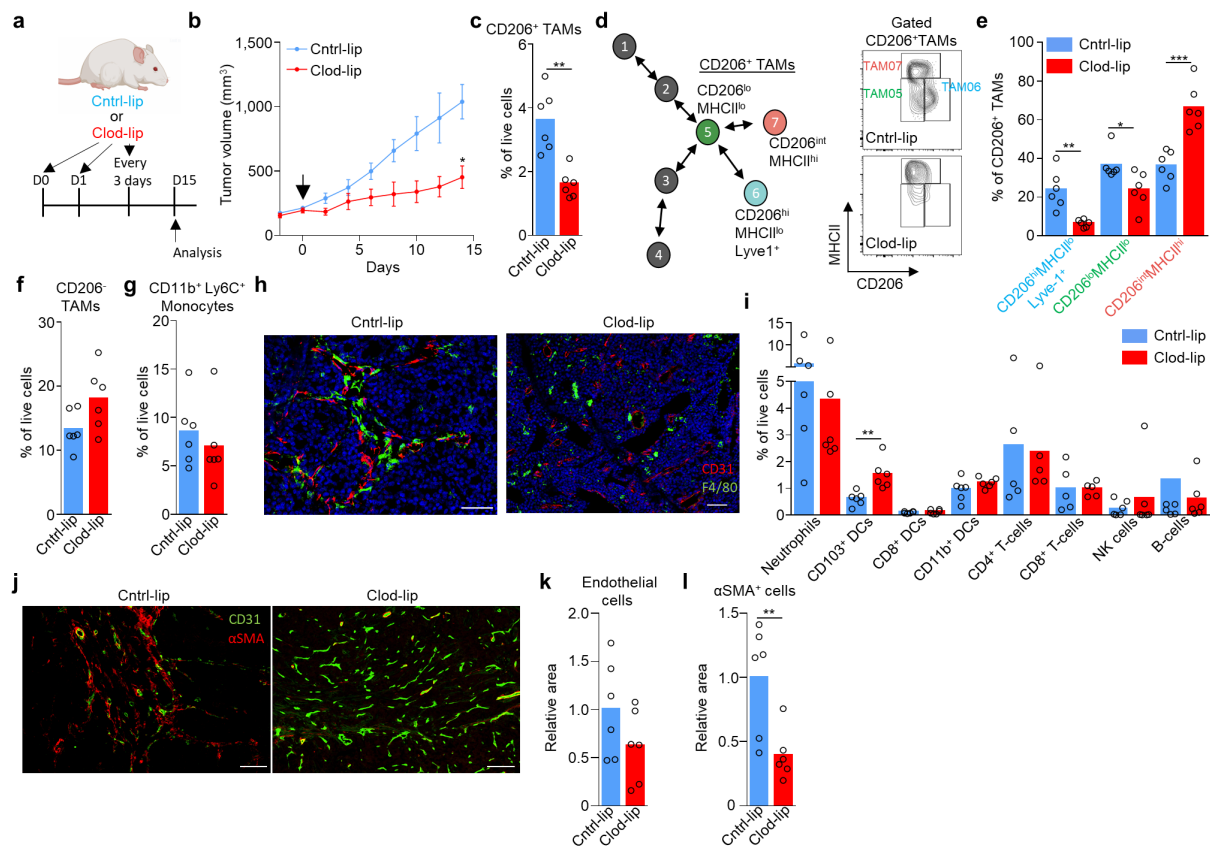
Fig. 3: Lyve-1+ PvTAM depletion slows tumor growth and is associated with a loss of αSMA+ Pv stromal cells. (**a**) Schematic for experimental approach and dosing strategy to deplete Lyve-1+ TAMs using clodronate-filled liposomes. Arrows represent days of treatment. (**b**) Growth curves of *MMTV-PyMT* tumors in mice treated with control PBS-filled liposomes (Cntrl-lip) or clodronate-filled liposomes (Clod-lip) as shown in panel (**a**), arrow marks the initiation of treatment, (cohorts of n=6 mice). (**c-i**) Tumors were excised at day 15 post initiation of administration of clodronate-filled liposomes shown in (**b**), enzyme-dispersed and assessed using flow cytometry (n=6 tumors in each condition) for; (**c**) Abundance of live (7AAD-) CD45+Ly6C-F4/80+CD206+ TAMs from enzyme-dispersed *MMTV-PyMT* tumors measured by flow cytometry. (**d**) Schematic of CD206+ TAM clusters identified in scRNA-seq (left in color), and a representative flow cytometry contour plots showing both cntrl- and clodronate-filled liposome treated tumors demonstrating depletion of CD206hiMHCIIlo(Lyve-1+) TAMs within the CD45+Ly6C-F4/80+ TAM gate (right) and (**e**) their quantification. (**f**) Abundance of live (7AAD-) CD45+Ly6C-F4/80+CD206- TAMs and (**g**) live CD45+CD11b+Ly6C+ monocytes. (**h**) Representative images of frozen sections of tumor sections from mice treated with cntrl- or clodronate-filled liposomes stained with DAPI (nuclei; blue) and antibodies against F4/80 (green) and CD31 (red). Scale bar represents 50μm (left panel) and 100μm (right panel). (**i**) The abundance of major immune cell types in the tumor microenvironment measured by flow cytometry. (**j-l**) Representative images of frozen sections of *MMTV-PyMT* tumors from mice treated with cntrl- or clodronate-filled liposomes stained with antibodies against CD31 (green) and αSMA (red), scale bar represents 100μm (left and right panels) (**j**) and the quantification of relative CD31+ pixel area (**k**) and αSMA+ pixel area (**l**), n=12 sections were analyzed from each of the 6 tumors in each cohort. Growth curve in (**b**) is presented as mean ± s.e.m and bar charts represent mean and the dots show individual data points from individual tumors and mice. * $P<0.05$, ** $P<0.01$, ***$P<0.001$.
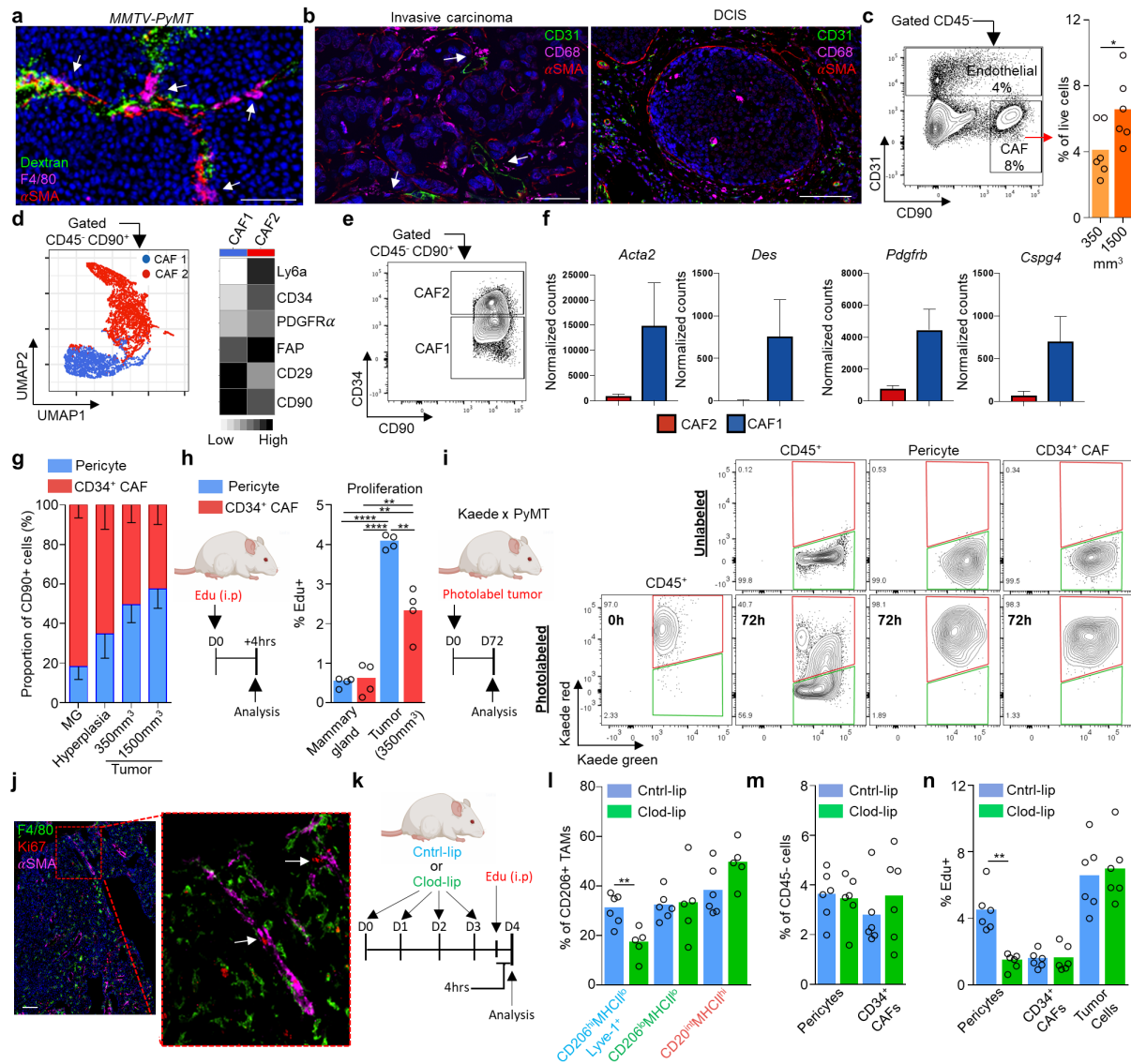
27

Fig. 4: Lyve-1⁺ PvTAMs orchestrate local pericyte expansion within the tumor. (**a**) Representative images of frozen sections of *MMTV-PyMT* tumors stained with DAPI (nuclei; blue) and antibodies against F4/80 (magenta) and αSMA (red); functional vasculature was labelled *in vivo* using i.v. dextran-FITC (green). Scale bar represents 100μm.
(**b**) Representative images of frozen sections from human invasive ductal mammary carcinoma (left) and DCIS (right) stained with DAPI (nuclei; blue) and antibodies against CD31 (green), CD68 (magenta) and αSMA (red), images representative of 5 patients. Scale bar represents 100μm (left panel) and 50μm (right panel). (**c**) Representative flow cytometry gating strategy for live (7AAD⁻) CD45⁻ cells and CD31⁺ endothelial cells and CD90⁺ CAFs (left) and the abundance of CAFs at different tumor volumes (right), n=6 mice per condition. (**d**) Identification of CAF subsets by unsupervised clustering from multiparametric flow cytometry data using the *FlowSOM* algorithm. UMAP and unsupervised clustering was performed using the markers shown in the heatmap (right). UMAP plot shows individual cells colored by their unsupervised clustering assignment (left). Heatmap displays the relative marker expression of each marker among the two subsets (right), n=4 mice. (**e**) Representative gating strategy for flow cytometry sorting the predicted subsets of CAFs by unsupervised clustering analysis. (**f**) Bar plots depicting normalized gene expression values for the indicated genes in the two bulk RNA-sequenced CAF subsets (across n=5 mice), showing that the αSMAʰⁱ CAFs expresses pericyte markers (*Des*, *Pdgfb and Cspg4*). (**g**) Abundance of the respective CAF populations during distinct stages of tumor progression, n=6 mice per stage. (MG; mammary gland). (**h**) Schematic for experimental approach and

28

dosing Edu into *MMTV-PyMT* mice to asses *in vivo* proliferation (left), proportion EdU$^+$ cells within each CAF subset (right). (**i**) Established tumors in *Kaede MMTV-PyMT* mice were photoconverted to kaede red and then at 72h post photoconversion tumors were analyzed (schematic left) for their respective kaede red/green proportion using flow cytometry for evidence of peripheral recruitment (Kaede green cells). A representative unconverted tumor is shown for comparison (right top). (**j**) Representative images of frozen sections of *MMTV-PyMT* tumors stained with antibodies against F4/80 (green), αSMA (magenta) and the proliferation marker Ki67 (red). White arrows show αSMA$^+$Ki67$^+$ cells in contact with F4/80$^+$ PvTAMs. (**k**) Schematic for experimental approach and dosing strategy to acutely deplete Lyve-1$^+$ PvTAM with clodronate-filled liposomes. (**l**) Abundance of TAM CD206$^+$TAM populations following cntrl- or clodronate-filled liposome treatment (n=6 mice cntrl-lip and n=5 mice clod-lip). (**m**) Abundance of CD45$^-$ cell populations (cohorts of n=6 mice). (**n**) Proportion of EdU$^+$ cells within each CD45$^-$ cell subset, (cohorts of n=6 mice). Bar charts represent mean, error bars represent s.d. and the dots show individual data points from individual tumors and mice. * $P<0.05$, ** $P<0.01$, ***$P<0.001$.
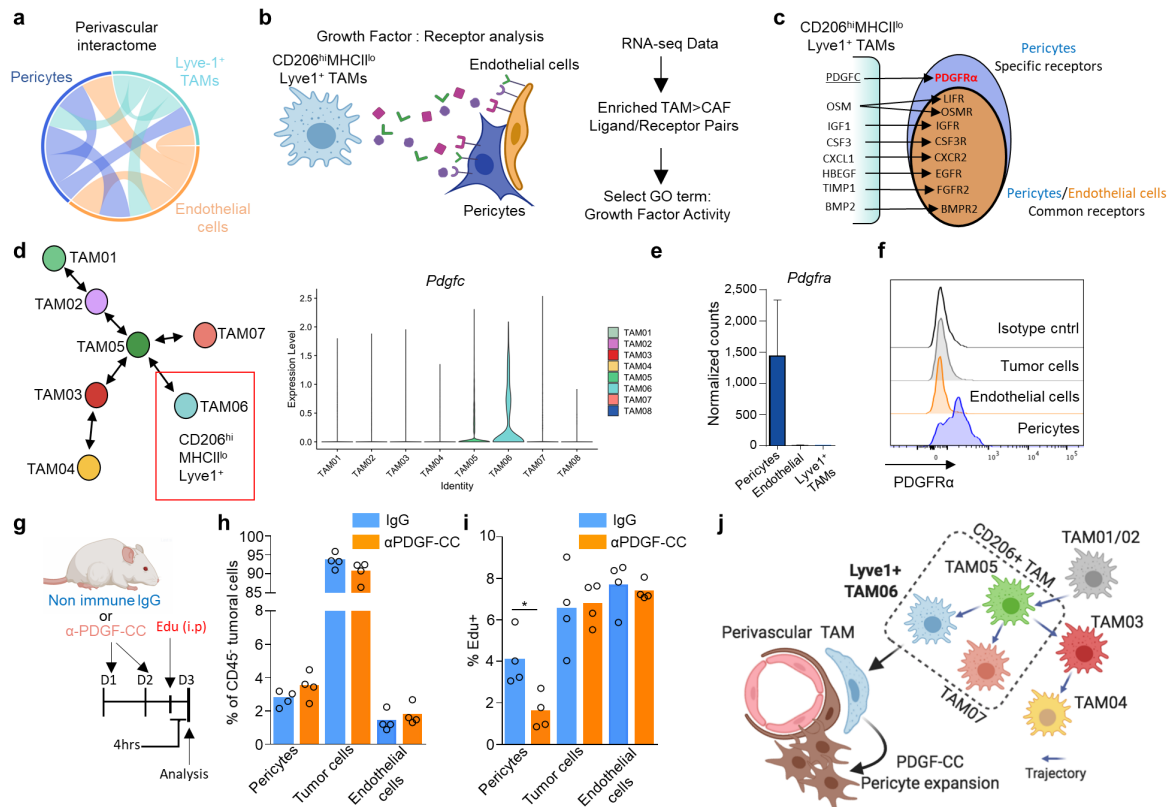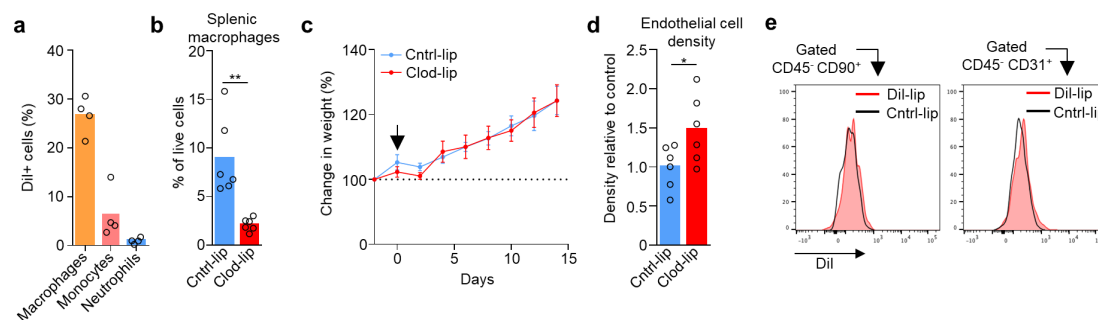
29

Fig. 5: Lyve-1+ PvTAMs crosstalk with pericytes and mediate PDGF-CC-dependent pericyte expansion. (**a**) Circos plot showing predicted crosstalk of perivascular ligand-receptor interactions as identified by *CellPhoneDB* from the respective RNA-seq datasets. Outer sectors and links between sectors are weighted according to the total number of annotated ligand-receptor interactions between each respective cell type. (**b**) Schematic representing the method of cell type ligand-receptor interactome generation. (**c**) Summary of the CD206+MHCIIloLyve-1+(TAM06) and αSMAhi pericyte population-specific secretome generated using data from (**a**) and the method outlined in (**b**) diagram displaying the ligand:receptor pairs between CD206+MHCIIloLyve-1+(TAM06) and αSMAhi pericytes and endothelial cells. The analysis highlighted in red represents a unique PDGF-CC:PDGFRα interaction specific to CD206+MHCIIloLyve-1+(TAM06) and αSMAhi pericytes. (**d**) Schematic map of each TAM cluster's location along the respective trajectories marking the CD206hiMHCIIloLyve-1+ population (left) and violin plots of *Pdgfc* expression associated with TAM clusters (right) (**e**) Bar plot depicting normalized gene expression values for *Pdgfra* in the bulk RNA-sequenced populations (left) across n=5 mice. (**f**) Representative histograms of surface PDGFRα staining on the indicated cells against isotype antibody staining of gated using flow cytometry analysis from enzyme-dispersed *MMTV-PyMT* tumors. (**g-i**) Schematic for experimental approach and dosing strategy to acutely inhibit PDGF-CC signalling using an anti-PDGF-CC neutralizing antibody (**g**). Abundance of indicated cell populations (**h**). Proportion of EdU+ cells within each CD45- cell subset, (cohorts of n=4 mice) (**i**). (**j**) Schematic overview of the Lyve-1+MHCIIloCD206hi supporting niche to support pericyte expansion through its selective expression of PDGF-CC. Images in panel (b and j) was created using *BioRender* software. Bar charts represent mean and the dots show individual data points from individual tumors and mice, error bars represent s.d. * *P*<0.05.

30

Supplementary Information
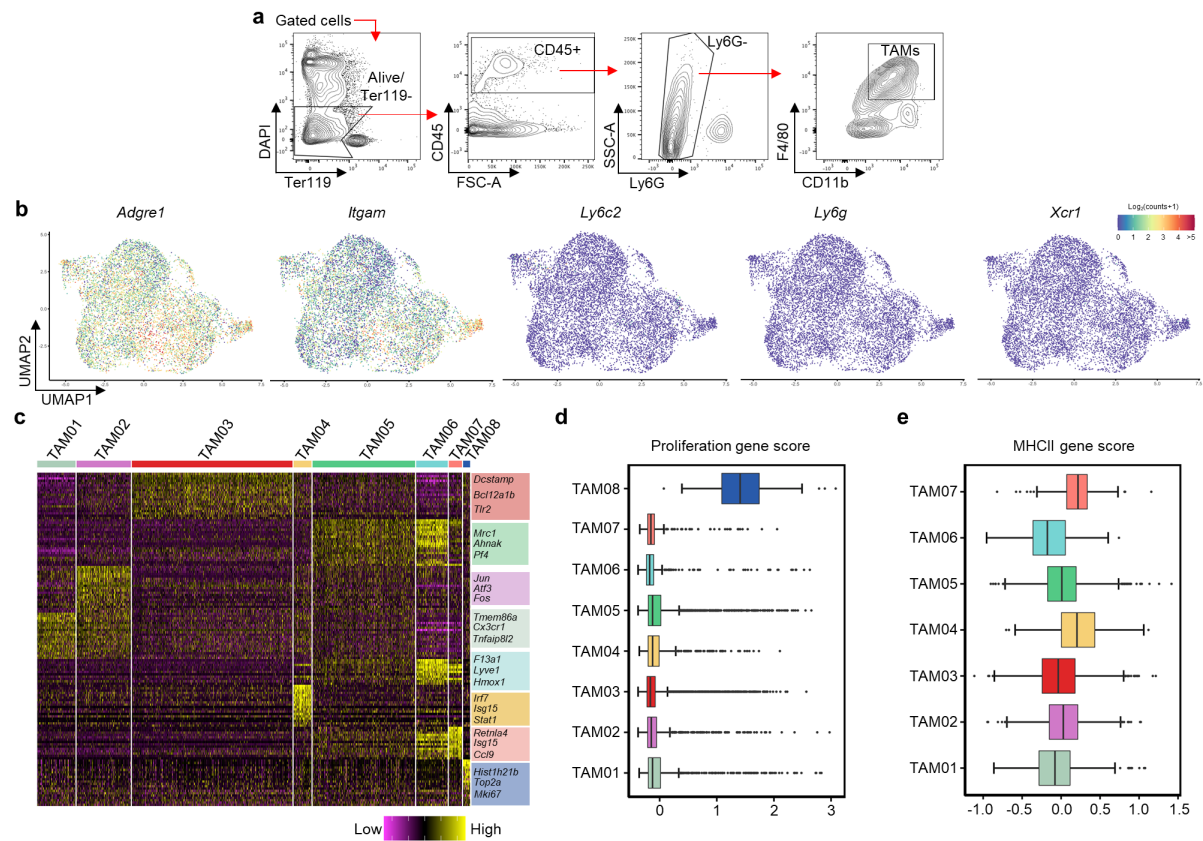
Supplemental Fig. 1: scRNA-seq of TAMs identifies distinct polarization states within the tumor microenvironment. (**a**) Representative gating strategy for live (7AAD⁻) TAMs for sorting using the indicated surface markers from enzyme-dispersed *MMTV-PYMT* tumors used in scRNA-seq sample preparation analyzed in Fig. 1 and 2. (**b**) UMAP plots of the 9,039 TAMs sequenced using the 10X Genomics' Chromium platform across n=3 tumors displaying the expression of marker genes used to isolate TAM single cells in (**a**). (**c**) Heatmap showing top differentially expressed genes within each TAM cluster shown in Fig.1b, selected genes for each cluster are highlighted to the right of the heatmap. (**d,e**) Gene scores across all TAM clusters for proliferation (**d**) and MHCII associated genes (**e**). Box and whisker plots, the boxes show median and upper and lower quartiles and whiskers shows the largest value no more than 1.5*IQR of the respective upper and lower hinges, outliers beyond the end of the whisker are plotted as individual dots.

Supplemental Fig. 2: Trajectory analysis of scRNA-seq of TAMs reveals polarization-specific transcription factors and cytokine signatures associated with transcriptomic state. (**a**) Diffusion component (DC) plot showing single cells colored by pseudotime value for each distinct trajectory predicted by *Slingshot* trajectory analysis. Cells that are not associated with a given trajectory are greyed out. (**b**) Heatmap of selected genes varying significantly across trajectory. Single cells (columns) are arranged left to right by pseudotime value within their labelled trajectories, branching points are indicated beneath the heatmap. (**c-e**) Heatmaps representing chemokine, cytokine and complement factor genes (**c**), transcription factor genes (**d**) and additional chemokine, cytokine and complement receptor genes (**e**) that vary significantly across the predicted *Slingshot* trajectories.

Supplemental Fig. 3: Liposomes are specifically taken up by a PvTAM subset of TAM.
(**a**) Proportion of live (7AAD$^-$) gated tumor-resident phagocytic populations with detectable Dil uptake as assessed using flow cytometry (n=4 mice). (**b-d**) Tumor bearing *MMTV-PyMT* mice treated with control PBS-filled liposomes (Cntrl-lip) or clodronate-filled liposomes (Clod-lip) using the treatment regimen shown in Fig. 3a, showing abundance of splenic live (7AAD$^-$) CD45$^+$CD11b$^+$Ly6c$^-$F4/80$^+$ macrophages (**b**), percentage change in mouse weight over the course of the experiment (**c**), and number of CD31$^+$ endothelial vessel elements as assessed using immunofluorescence analysis stained frozen tissue sections (n=12 sections/tumor) (**d**) (n=6 mice per condition). (**e**) Representative histograms showing Dil-containing liposome uptake (red filled histogram) against PBS-filled liposome treated mice (open black line histogram) in CD90$^+$ CAF and CD31$^+$ endothelial cells in the CD45$^-$ gate of enzyme-dispersed tumors from *MMTV-PyMT* mice treated as shown in Fig. 2j and assessed using flow cytometry, representative of n=3 mice. Bar charts represent mean and the dots show individual data points from individual tumors and mice. * *P*<0.05, ** *P*<0.01.
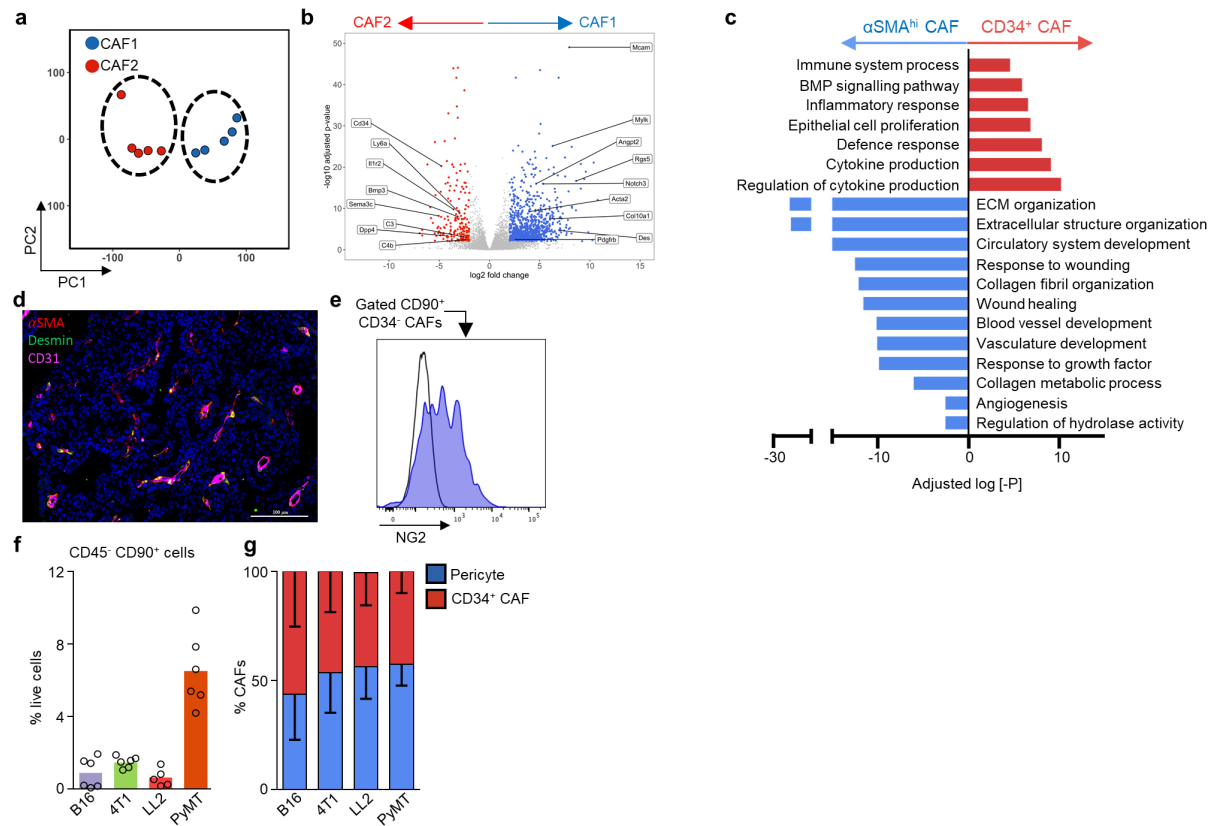
Supplemental Fig. 4: CD34$^{+/-}$ CAF subsets are transcriptionally distinct and conserved across other murine models of cancer. (**a-c**) Bulk RNA-seq of the CD34$^{+/-}$CAF subsets, showing PCA plot of the bulk-sequenced CAF populations showing the difference in CAF transcriptome (**a**), differentially expressed genes between CD34$^{+/-}$ CAF populations (**b**) and significantly upregulated GO terms based on differentially expressed genes of the two CAF subsets (**c**), across n=5 tumors and mice. (**d**) Representative confocal image of frozen *MMTV-PyMT* tumor sections showing DAPI (nuclei; blue), and antibody staining against CD31 (magenta), αSMA (red) and Desmin (green). Representative of multiple sections from n=4 tumors and mice. Scale bar represents 100μm. (**e**) Representative histogram of live (7AAD$^-$) CD90$^+$CD34$^-$ CAFs gated using flow cytometry in a representative enzyme-dispersed MMTV-PyMT tumor; histogram shows surface PDGFRα staining (blue shaded) against that of the isotype control (open). (**f-g**) Mice were injected with the indicated tumor cells and when tumors reached 1500mm^3 they were enzyme-dispersed and analyzed by flow cytometry for the abundance of live (7AAD$^-$) CD45$^-$CD31$^-$CD90$^+$ CAFs (**f**) and the relative proportions of CD34$^+$CAFs and CD34$^-$ pericytes (**g**) across n= 5-6 mice per model. Bar charts represent mean and error bars s.d., dots show individual data points from individual tumors and mice.
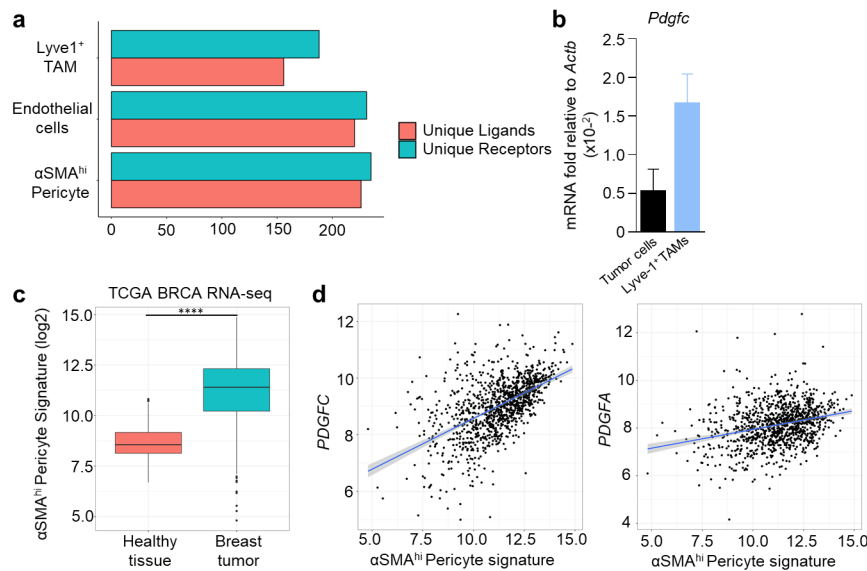
Supplemental Fig. 5: An αSMA pericyte signature correlates with *PDGFC* expression in human breast cancer (**a**) The number of unique ligand and receptor molecules identified that participate in paracrine signaling networks in the perivascular niche per cell type. (**b**) *Pdgfc* mRNA expression relative to the housekeeping gene *Actb* in FACS-sorted tumor cells (CD45⁻CD31⁻CD90⁻ ; n=6) and Lyve-1⁺ TAMs (n=3). (**c**) Normalized log2 RNA-seq counts for the TCGA-BRCA dataset for the αSMAhi pericyte gene signature in non-malignant breast tissue (n=112) and primary breast carcinoma tissue (n=1,093). (**d**) Scatterplot of αSMAhi pericyte gene signature score (x axis) and *PDGFC* (y axis) (Pearson's r = 0.547, p < 0.0001) (left) or *PDGFA* (y-axis) (Pearson's r = 0.286 p < 0.0001) (right) from the TCGA-BRCA RNA-seq dataset, n=1093. Box and whisker plots, the boxes show median and upper and lower quartiles and whiskers shows the largest value no more than 1.5*IQR of the respective upper and lower hinges, outliers beyond the end of the whisker are plotted as individual dots. Bar charts represent mean, error bars represent s.e.m. **** *P*<0.0001.